SCIENCE CHINA Materials ARTICLES

mater.scichina.com link.springer.com

Published online 13 October 2020 | https://doi.org/10.1007/s40843-020-1468-6

Sci China Mater 2021, 64(3): 557–570

Sodium ion storage performance and mechanism in orthorhombic V_2O_5 single-crystalline nanowires

Yanwei Li[1,2], Jingcheng Ji[1], Jinhuan Yao[1*], Ying Zhang[1], Bin Huang[1] and Guozhong Cao[2*]

ABSTRACT **A fundamental understanding of the electrochemical reaction process and mechanism of electrodes is very crucial for developing high-performance electrode materials. In this study, we report the sodium ion storage behavior and mechanism of orthorhombic V_2O_5 single-crystalline nanowires in the voltage window of 1.0–4.0 V (*vs.* Na/Na^+). The single-crystalline nanowires exhibit a large irreversible capacity loss during the first discharge/charge cycle, and then show excellent cycling stability in the following cycles. At a current density of 100 mA g^{-1}, the nanowires electrode delivers initial discharge/charge capacity of 217/88 mA h g^{-1}, corresponding to a Coulombic efficiency of only 40.5%; after 100 cycles, the electrode remains a reversible discharge capacity of 78 mA h g^{-1} with a fading rate of only 0.09% per cycle compared with the 2nd cycle discharge capacity. The sodium ion storage mechanism was investigated, illustrating that the large irreversible capacity loss in the first cycle can be attributed to the initially formed single-crystalline α'-$Na_xV_2O_5$ ($0.02 < x < 0.88$), in which sodium ions cannot be electrochemically extracted and the α'-$Na_{0.88}V_2O_5$ can reversibly host and release sodium ions *via* a single-phase (solid solution) reaction, leading to excellent cycling stability. The Na^+ diffusion coefficient in α'-$Na_xV_2O_5$ ranges from 10^{-12} to $10^{-11.5}$ cm^2 s^{-1} as evaluated by galvanostatic intermittent titration technique (GITT).**

Keywords: sodium ion batteries, V_2O_5, single-crystalline, nanowires, sodium storage mechanism

INTRODUCTION

Currently, lithium-ion batteries (LIBs) are widely employed in portable electronic devices, electrical vehicles, and grid energy storage due to their high-power density, large energy density, and long lifespan [1,2]. However, the low abundance (only 0.0017 wt% in the earth's crust) of Li resource is a great obstacle for the massive development of LIBs in large-scale energy storage applications [3]. In this context, sodium-ion batteries (SIBs) are expected to be one of the most promising candidates for post LIBs because of the abundant resource of Na (~2.83 wt% in the earth's crust) and the similar chemical properties of Na and Li [4,5]. The radius of Na^+ (1.02 Å) is much larger than that of Li^+ (0.76 Å), which leads to sluggish sodiation/desodiation reaction kinetics and poor cycling performance. The exploration of high-performance electrodes is crucial for the development of SIBs [6,7]. To date, a large number of cathode materials, including layered transition-metal oxides [8], polyanion cathodes [9], Prussian blue analogs [10], and organic compounds [11] for SIBs have been explored. Among these potential cathode materials for SIBs, vanadium oxides have attracted more attention owing to their open frameworks, rich oxidation states of V (from V^{2+} to V^{5+}), high theoretical capacities, and abundant source [12–17]. As a classical layered intercalation host, V_2O_5 provides a good model structure for exploring the structure/electrochemical performance relationship of electrode materials [18]. Ali *et al.* [19] investigated the Na^+ intercalation mechanism in nanosized V_2O_5/C composite in a voltage range of 1.2–4.0 V (*vs.* Na/Na^+). However, the detailed structural information of the intermediate phases upon Na^+ intercalation and deintercalation processes was not provided. The V_2O_5/C composite gave a much lower initial discharge capacity than the initial charge capacity, which contradicts the results of pure V_2O_5 materials [20–23]. Most of the previous investigations focused on polycrystalline and defective/amorphous V_2O_5 systems. Both amorphous and single-crystalline structures have the same/similar structure over short range in terms of bond length and coordination numbers. Compared with

[1] Guangxi Key Laboratory of Electrochemical and Magneto-chemical Functional Materials, College of Chemistry and Bioengineering, Guilin University of Technology, Guilin 541004, China
[2] Department of Materials Science and Engineering, University of Washington, Seattle, WA 98195, United States
* Corresponding authors (emails: yaojinhuan@126.com (Yao J); gzcao@uw.edu (Cao G))

polycrystalline and amorphous structures, single-crystalline structure has no grain boundary and few structural defects and, thus provides an ideal benchmark model for investigating the intrinsic structure/performance relationship and reaction/transport mechanism of materials. The rationale of the single-crystalline V_2O_5 for battery electrodes could offer a scientific understanding of what is the fundamental reason or one of the fundamental reasons leading to a less desirable electrochemical performance. Up to now, there is no report on the sodium ion storage performance of single-crystalline V_2O_5 material.

In the present work, the sodium-ion storage property of the V_2O_5 single-crystalline nanowires was investigated and the reason hindering the performance was analyzed in detail. According to the *ex-situ* X-ray diffraction (XRD), scanning electron microscopy (SEM), and transmission electron microscopy (TEM) analyses, the initial Na^+ intercalation into V_2O_5 single-crystalline nanowires induces an irreversible phase transition from α-V_2O to α'-$Na_xV_2O_5$ (x<0.88), in which Na^+ cannot be electrochemically extracted, thus leading to a large irreversible capacity loss during the initial discharge/charge cycle; Na^+ can be reversibly inserted into the α'-$Na_{0.88}V_2O_5$ *via* a single-phase reaction with negligible variation of the interlayer distance of the host structure. The electrochemical reaction kinetics was evaluated by means of cyclic voltammetry (CV), electrochemical impedance spectroscopy (EIS), and galvanostatic intermittent titration technique (GITT) techniques. It demonstrates that the sodium-ion storage reaction in α'-$Na_xV_2O_5$ is mainly controlled by diffusion-controlled process and the Na^+ diffusion coefficient ranges from 10^{-12} to $10^{-11.5}$ $cm^2\ s^{-1}$. This study sheds light on why the performance of singe-crystalline V_2O_5 is worse, and thus pushes the researchers to find ways to avoid or prevent such irreversible phase transition.

EXPERIMENTAL SECTION

Preparation of orthorhombic V_2O_5 nanowires

The orthorhombic V_2O_5 nanowires were synthesized by a hydrothermal method. In a typical procedure, 0.255 g of commercial V_2O_5 powder was dispersed in 4.28 mL of deionized (DI) water; then 0.72 mL of 30% H_2O_2 was added to the above dispersion and vigorously stirred for 20 min to form a transparent orange-red solution. The resulting solution was further diluted by adding 45 mL of DI water and then transferred into a 100-mL Teflon lined stainless autoclave. The autoclave was sealed and maintained at 160°C for 12 h. After reaction, the yellow precipitates were collected by centrifugation and washed with DI water several times. Finally, the collected precipitate was freeze-dried to constant weight and annealed at 200°C for 2 h in air to obtain the orthorhombic V_2O_5 nanowires.

Material characterization

The phase structure of the samples was studied by an X-ray diffractometer (XRD, X'Pert^3 Powder, Panalytical, Netherlands) with Cu Kα radiation (λ = 1.5406 Å). The morphology and detailed microstructure of the samples were observed by field-emission SEM (FESEM, SU-5000, Hitachi, Japan) and high-resolution TEM (HRTEM, JEM-2100Plus, JEOL, Japan). The composition and valance state of V in the samples were analyzed by X-ray photoelectron spectroscopy (XPS, ESCALAB 250Xi, Thermo Fisher Scientific, USA) with Al Kα X-ray as the excitation source.

Electrochemical measurements

All electrochemical measurements were performed using CR2016 coin-type cells at room temperature. The working electrodes were fabricated by mixing the as-prepared V_2O_5 nanowires (70 wt.%), super-P carbon black (20 wt.%), and polyvinylidene difluoride (PVDF, 10 wt.%) in *N*-methyl-2-pyrrolidone (NMP) to form a homogeneous slurry; the slurry was spread onto an Al foil and then dried in a vacuum oven at 80°C; finally, the Al foil was punched into disks with a diameter of 16 mm and served as working electrode (the areal loading was ~0.7 mg cm^{-2}). Metallic Na foil (99.7%, Aladdin) was used as a counter electrode, and 1 mol L^{-1} $NaClO_4$ in ethylene carbonate (EC) and propylene carbonate (PC) (1:1 in volume) was used as the electrolyte. Whatman glass fiber membrane (Whatman GF/D) was used as a separator. All the coin cells were assembled in a high purity Ar-filled glove box (H_2O<1 ppm, O_2<1 ppm). CV and EIS measurements were performed on a CHI760E electrochemical workstation. For EIS measurement, the frequency was between 100 kHz and 0.01 Hz with alternating current (AC) amplitude of 5 mV. Galvanostatic discharge/charge tests of the cells were carried out in a voltage range of 1.0–4.0 V (*vs.* Na/Na^+) *via* a multichannel battery testing system (Neware, BTS-5V/10mA). As for the *ex-situ* XRD, SEM, and TEM measurements, the coin cells at different discharge/charge states were disassembled in an Ar-filled glove box. Then, the disassembled electrodes were thoroughly washed with PC to remove the residual salt from the electrolyte, dried, and

sealed in polypropylene bottles to avoid further reaction with air and/or moisture before physical characterizations. GITT measurement was also performed on the multi-channel battery testing system (Neware, BTS-5V/10mA), where the cell was tested at a pulse current of 20 mA g^{-1} for 15 min between 40 min rest intervals.

RESULTS AND DISCUSSION

Microstructures of the as-prepared sample

Fig. 1a presents the XRD pattern of the as-prepared sample. All the diffraction peaks can be well indexed to the orthorhombic V_2O_5 phase (JCPDS, No. 41-1426). The intense peaks show a high degree of crystallinity. The calculated lattice parameters of the as-prepared sample are a =11.505 Å, b = 3.567 Å, and c= 4.369 Å, which are in good agreement with the literature values [24–27]. The V $2p_{3/2}$ XPS spectrum (Fig. S1a) of the as-prepared sample is composed of two components: the major peak at 517.05 eV and the shoulder peak at 515.78 eV, which can be ascribed to V^{5+} and V^{4+}, respectively [28]. The molar ratio of $V^{4+}/(V^{5+}+V^{4+})$ is determined to be 10.3%. As shown in Fig. 1b, c, the V_2O_5 sample consists of smooth nanowires with the lengths of hundreds of micrometers and diameters ranging from 100 to 500 nm. The low-magnification TEM images (Fig. 1d, e) further confirm the long nanowire morphology. The selected area electron diffraction (SAED) image (Fig. 1f) verifies that the as-prepared V_2O_5 nanowires are single crystalline and grow along [010] direction. Fig. 1g shows the HRTEM image, in which the clear lattice fringes with interplanar spacings of 0.36 and 0.44 nm correspond to the (010) and (001) planes of orthorhombic V_2O_5, respectively.

The formation process of this single-crystalline V_2O_5 nanowires can be described as follows: firstly, V_2O_5 powders dissolve in DI water by reacting with H_2O_2 to form the orange-red solution (Equations (1–5)) [29,30]; upon hydrothermal treatment, the $[H_2V_{10}O_{28}]^{4-}$ undergoes condensation and forms the solid nucleus of crystalline V_2O_5 nanostructures (Equation (6)); since [010] direction is the fastest growing direction for V_2O_5 crystal growth [31–33], the initially formed nucleus induces surface condensation of $[H_2V_{10}O_{28}]^{4-}$ on the energetically favorable (010) surface and finally results in the formation of ultralong single-crystalline nanowires (Fig. 1b, c). Note that only commercial V_2O_5 powders, DI water, and H_2O_2 (without using any templates, organic surfactants, inorganic salts, and harmful solvents) are used in the synthesis process. Thus, the resulting V_2O_5 nanowires obtained in the present work have a high purity and crystallinity as compared with those reported in the literatures [31,34–37].

$$V_2O_5+4H_2O_2 \rightarrow 2\left[VO(O_2)_2(OH_2)\right]^-+2H^++H_2O, \quad (1)$$

$$V_2O_5+2H^++2H_2O_2+3H_2O \rightarrow 2\left[VO(O_2)(OH_2)_3\right]^+, \quad (2)$$

$$2\left[VO(O_2)_2(OH_2)\right]^-+4H^++2H_2O \rightarrow 2\left[VO(O_2)(OH_2)_3\right]^++O_2\uparrow, \quad (3)$$

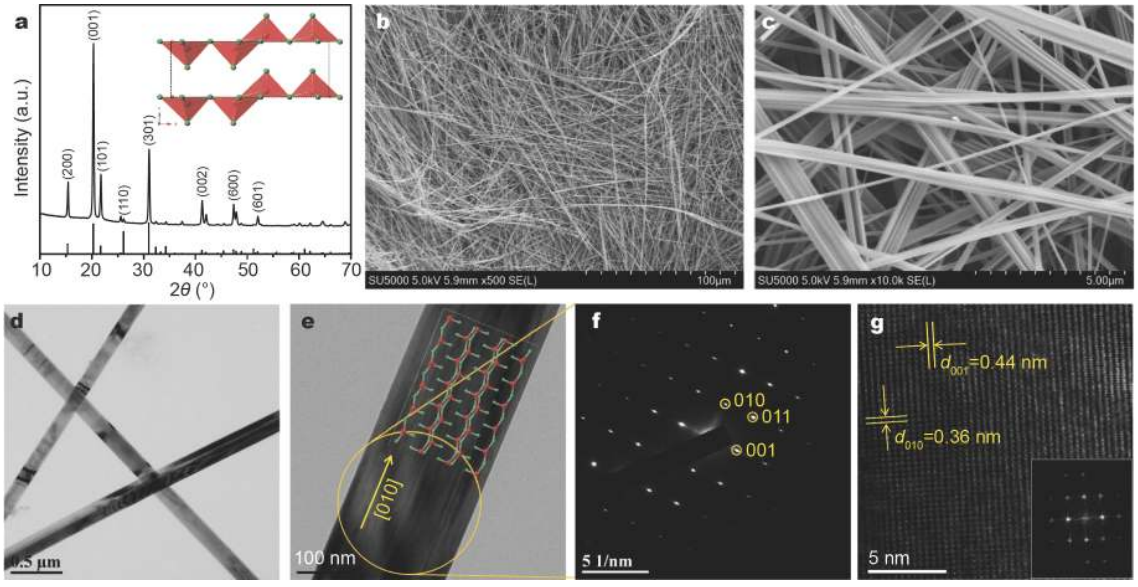

Figure 1 (a) XRD pattern, (b, c) SEM images, (d, e) TEM images, (f) SAED pattern, and (g) HRTEM image of the V_2O_5 nanowires obtained by hydrothermal growth followed by annealing at 200°C in air.

$$2[VO(O_2)(OH_2)_3]^+ \rightarrow 2[VO_2]^+ + 6H_2O + O_2 \uparrow, \quad (4)$$

$$10[VO_2]^+ + 8H_2O \leftrightarrow [H_2V_{10}O_{28}]^{4-} + 14H^+, \quad (5)$$

$$[H_2V_{10}O_{28}]^{4-} + 4H^+ \rightarrow V_2O_5 \text{ nanowires} + 3H_2O. \quad (6)$$

Sodium ion storage properties of the V_2O_5 single-crystalline nanowires

Fig. 2a displays the cycling performance of the V_2O_5 single-crystalline nanowires electrode at 100 mA g^{-1}. In the first discharge/charge cycle, the discharge capacity is 217 mA h g^{-1}, while the charge capacity is only 88 mA h g^{-1}, corresponding to a Coulombic efficiency (CE) of only 40.6%. The $V^{4+}/(V^{4+}+V^{5+})$ molar ratio in the fully charged V_2O_5 is estimated to be 46.7% (Fig. S1b), much higher than that (10.3%) in the as-prepared V_2O_5 sample. This further verifies that a large amount of Na^+ ions are trapped in the lattice of active material upon the initial discharge/charge cycle. In the subsequent cycles, the discharge capacity becomes stable and the CE immediately increases close to 100%; after 100 cycles, the electrode retains a reversible discharge capacity of 78 mA h g^{-1}, with a fading rate as low as 0.09% per cycle compared with the 2nd cycle discharge capacity. Fig. 2b presents the discharge/charge voltage profiles in the selected cycles at 100 mA g^{-1}. Obviously, the electrode experiences a large irreversible capacity loss during the first discharge/charge cycle. In the first discharge process, the voltage profile shows three plateaus at about 2.0, 1.73, and 1.31 V, respectively, implying that the intercalation of Na^+ in V_2O_5 single-crystalline nanowires consists of three steps. Similar discharge profiles were also observed for commercial V_2O_5 micro grains (0.5 μm × 0.5 μm × 1.0 μm) [23] and aggregated V_2O_5 particles (200–500 nm) [38]. The discharge plateaus at 2.0, 1.73, and 1.31 V (*vs.* Na/Na^+) for Na^+ intercalation is 1.4, 1.47, and 1.04 V lower than those (3.4, 3.2, and 2.35 V *vs.* Li/Li^+) for Li^+ intercalation in orthorhombic V_2O_5 [39]. In the first charge process, the voltage profile exhibits one plateau at ~1.85 V followed by a progressively increasing slope up to 4.0 V. With the cycle number increasing from the 2nd to 100th cycles, both the discharge and charge potentials shift to higher voltages due to the formation of a surface layer and local structural rearrangement of active materials during cycling [22,23].

Fig. 2c presents the Nyquist plots of the electrode before cycling and after different discharge/charge cycles at 100 mA g^{-1}. Before cycling, the EIS plot shows only one depressed semicircle and an inclined line, which relate to charge transfer resistance (R_{ct}) at the electrode/electrolyte

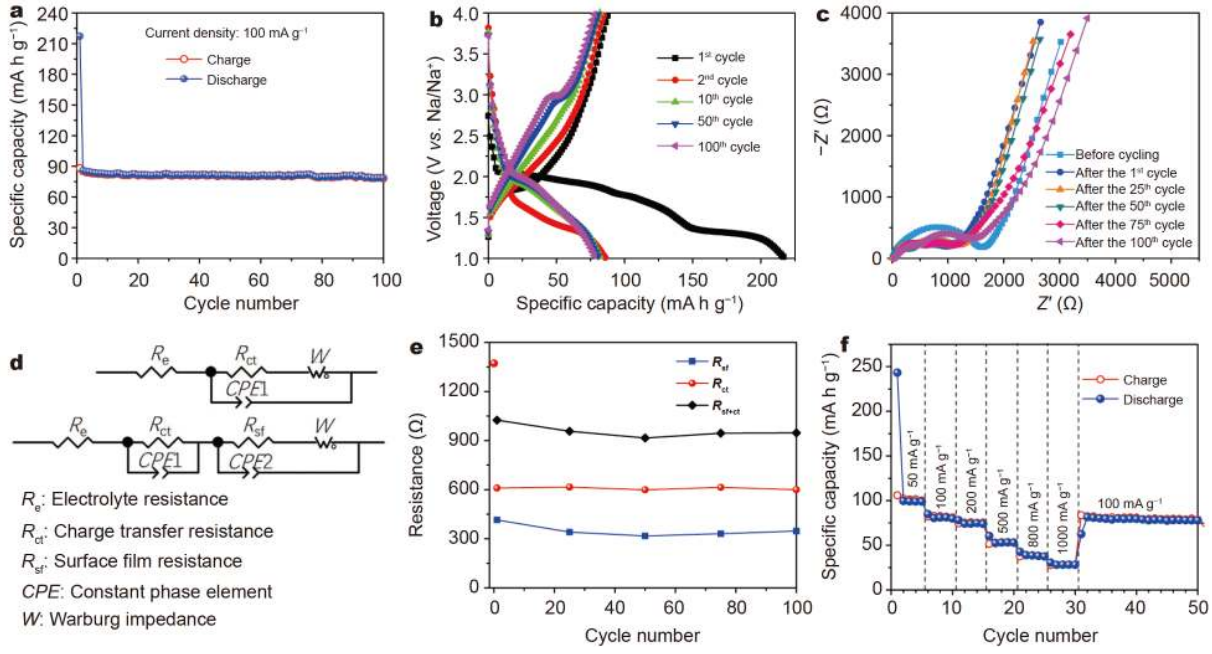

Figure 2 (a) Cycling performance and (b) the selected discharge/charge profiles in different cycles of the V_2O_5 nanowires electrode at the current density of 100 mA g^{-1}. (c) Nyquist plots of the V_2O_5 nanowires electrodes before cycling and after different discharge/charge cycles. (d) The equivalent circuit models used for fitting the EIS plots. (e) The evolutions of R_{ct}, R_{sf}, as well as their sum (R_{sf+ct}) with increasing discharge/charge cycles at the current density of 100 mA g^{-1}. (f) Rate performance of the V_2O_5 nanowires electrode.

interface and Warburg impedance (Na^+ diffusion in electrode), respectively [40]; after the 1st discharge/charge cycle, there appears an additional depressed semicircle in the high frequency region, which can be assigned to the resistance (R_{sf}) of Na^+ migrating through the solid electrolyte interface (SEI) film [41]. The formation of SEI layer on the surface of the active material can be discerned from the TEM image of the electrode after the 1st discharge/charge cycle (Fig. S2). The EIS plots were fitted with the equivalent circuits (Fig. 2d) and the evolutions of R_{ct}, R_{sf} and their sum (R_{ct+sf}) with increasing cycle numbers are presented in Fig. 2e. Before cycling, the R_{ct} of the electrode is 1372 Ω. After the first cycle, the R_{ct} decreases to 610 Ω. This reduction of R_{ct} is commonly observed in other electrode materials for LIBs and SIBs, and is generally ascribed to the improved penetration of electrolyte into the electrode [42–46]. After the 1st discharge/charge cycle, the electrode shows a relatively stable R_{ct} (600–615 Ω), R_{sf} (320–415 Ω), and R_{ct+sf} (916–1025 Ω), implying a good stability during the repeated discharge/charge processes.

Fig. 2f gives the rate performance of the electrode at different current densities. The electrode delivers reversible capacities of 101, 81, 53, and 28 mA h g^{-1} at the current density of 50, 100, 500, and 1000 mA g^{-1}, respectively. The reversible capacity can recover to the original value when the current returns to 100 mA g^{-1}. As shown in Fig. S3, with the increase of current density, the discharge voltage decreases and the charge voltage increases gradually due to the growing polarization effect. The polarization effect during the charging process is more significant than that during the discharging process. The exact reason for the polarization difference between the charging and discharging processes is not fully clear now. However, there are some possible reasons: (i) the composition of the electrode is always changing during Na^+ intercalation and deintercalation processes. The change of chemical composition of the electrode results in the different polarization effects between charging and discharging processes. (ii) The difference in kinetics between charging and discharging processes leads to the different polarization effects. (iii) The counter electrode (electrodeposition and dissolution of metallic Na anode) may also influence the polarization of the half-cell during charging and discharging processes.

Table 1 compares the sodium ion storage performance of the as prepared V_2O_5 single-crystalline nanowires with the polycrystalline V_2O_5 samples reported in literatures. The V_2O_5 single-crystalline nanowires shows an initial CE of 40.6%, which is lower than that of the polycrystalline samples, such as hollow V_2O_5 microspheres (48.0%) [23], aggregated V_2O_5 particles (62.5%) [38], two-dimensional V_2O_5 nanosheets (~67%) [47], and V_2O_5 hollow nanospheres (72.9%) [21]. The initial CE of polycrystalline V_2O_5 could be further increased by decreasing the crystallinity and/or reducing the particle size. For example, the V_2O_5 nanobundles (with low crystallinity and thicknesses less than 20 nm) give an initial CE of 100.5% [23], and the ultra-fine V_2O_5 nanoparticles (5–7 nm) encapsulated in nanoporous carbon show an initial CE of 109.1% [48]. Particularly, the nanosized V_2O_5/C composite with low crystallinity due to ball-milling treatment exhibits an abnormal initial CE of 150.3% [19]. The first discharge capacity (195 mA h g^{-1}) is much lower than the first charge capacity (293 mA h g^{-1}). In the 10th cycle, the discharge capacity increases to 255 mA h g^{-1}, while the charge capacity is almost identical to the first charge capacity (293 mA h g^{-1}), corresponding to a CE of 115%. The authors ascribed the abnormal CE to the formation of the SEI layer during the charging process [19]. Thus,

Table 1 A comparison of the sodium ion storage performance of orthorhombic V_2O_5 materials from the literature

Electrode materials	Current density (mA g^{-1})	1st Discharge/charge capacity (mA h g^{-1})	Initial efficiency (%)	Reversible capacity (mA h g^{-1})	Ref.
V_2O_5 single-crystalline nanowires	100	217/88	40.6	78 after 100 cycles	This work
Hollow V_2O_5 microspheres (3–5 μm)	20	304/146	48.0	~112 after 5 cycles	[23]
Aggregated V_2O_5 particles (200–500 nm)	29.42	208/130	62.5	59.5 after 40 cycles	[38]
V_2O_5 nanosheets	100	170/114	~67	~20 after 30 cycles	[47]
V_2O_5 hollow nanospheres (less than 20 nm)	80	225/164	72.9	~118 after 100 cycles	[21]
V_2O_5 nanobundles (low crystallinity and the thicknesses below 20 nm)	20	195/196	100.5	~170 after 5 cycles	[23]
V_2O_5 nanoparticles (5–7 nm) encapsulated in nanoporous carbon	40	276/301	109.1	~268 after 20 cycles	[48]
Nanosized V_2O_5/C composite (low crystallinity due to ball-milling treatment)	14.7	195/293	150.3	243 after 30 cycles	[19]

there is a tradeoff between the increased reactivity associated with the low crystallinity of nanostructured V_2O_5 and the related side reactions. From the above comparison, the single-crystalline V_2O_5 has the lowest initial CE, and most of the intercalated sodium ions are trapped in single-crystalline V_2O_5 during the first discharge/charge processes; in contrast, polycrystalline V_2O_5 materials show much improved initial CE; especially, the initial CE of polycrystalline V_2O_5 can be further increased by reducing its particle size and/or crystallinity. The possible reasons causing such less desirable electrochemical properties of the single-crystal nanostructures is deserving more research; however, the possible reasons include: (i) surface and/or interface defects in bulk polycrystalline electrodes have been well reported and demonstrated in literature by multiple research groups to benefit the redox reaction, and (ii) bulk defects, impurities and imperfections in common bulk polycrystalline electrodes have also shown to promote and enhance the storage capacity and transport properties [49–51]. The present work adds a significant weight that proper surface and bulk imperfections are desirable to attain desired electrochemical properties and enhance the reaction and transport kinetics.

Fig. 3a shows the initial six consecutive CV curves of the electrode at a scan rate of 0.2 mV s^{-1}. The first cycle CV curve exhibits an intense reduction peak at ~1.80 V, a shoulder reduction peak at ~1.70 V, and an obvious reduction peak at ~1.17 V, indicating that the intercalation of Na^+ into V_2O_5 host occurs in three steps. In the reverse scan, only one obvious oxidation peak appears, demonstrating the large irreversible capacity loss during the initial sodiation/disodation processes. The above CV features are consistent with the previously reported results [23]. In the subsequent CV curves, the intense reduction peak at ~1.8 V disappears and the left redox peaks become broad and shift to high voltage side gradually, which will be discussed later. The above CV results are in good agreement with the discharge/charge profiles (Fig. 2b).

To determine the origin of the large irreversible capacity loss during the initial discharge/charge cycle, we performed CV measurement in a narrow voltage range of 1.4–4.0 V (*vs.* Na/Na^+) as shown in Fig. 3b. During the first cathodic scan, a broad reduction peak is in the potentials ranging from 2.15 to 1.40 V due to the intercalation of Na^+; however, no corresponding oxidation peak appears in the reverse anodic scan. The featureless and well-overlapped CV curves in the 2nd and 3rd cycles evidence a typical double-layer capacitive behavior of the

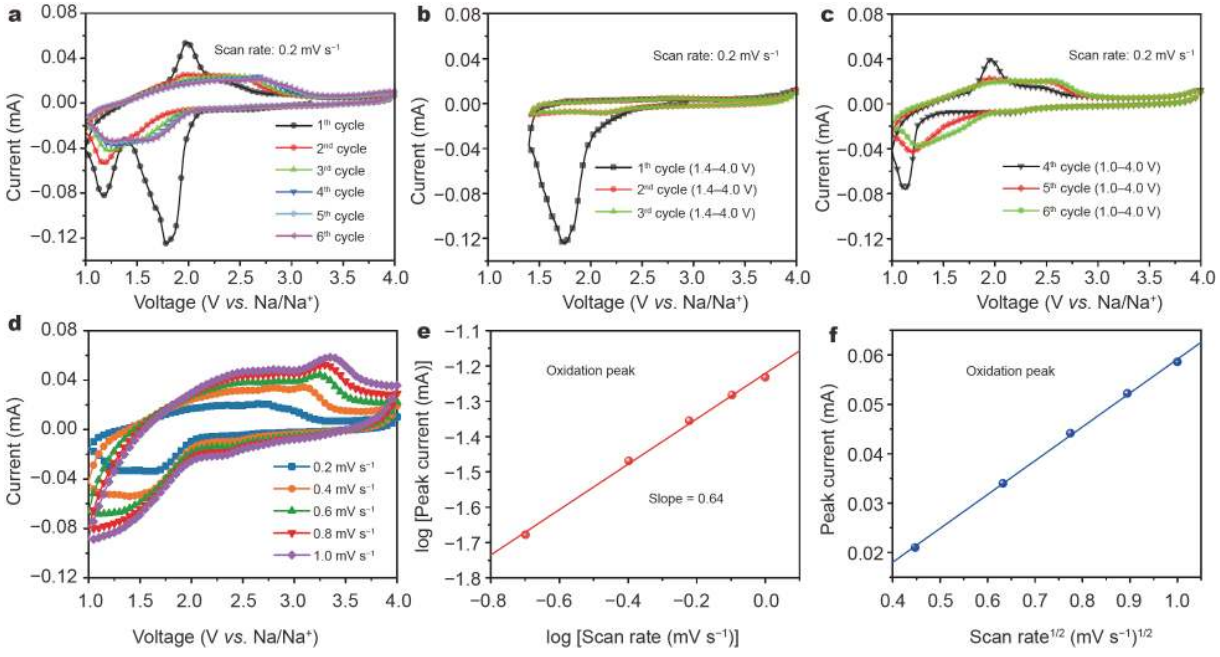

Figure 3 (a) CV curves of the V_2O_5 nanowires electrode in the voltage range of 1.0–4.0 V. (b, c) The six consecutive CV curves of the V_2O_5 nanowires electrode in the narrow voltage range of 1.4–4.0 V (from the 1st to 3rd cycle) and extended voltage range of 1.0–4.0 V (from the 4th to 6th cycle). (d) CV curves of the V_2O_5 nanowires electrode at various scan rates in the voltage range of 1.0–4.0 V. (e) log-log plots of the oxidation peak current (*i*) against the scan rate (*v*) and (f) the oxidation peak current (*i*) against the square root of scan rate ($v^{1/2}$) for the V_2O_5 nanowires electrode (symbols and lines represent the experimental data and fitted linear lines, respectively).

electrode, indicating that an irreversible phase transition occurs during the initial sodiation process in the voltage range of 1.4–4.0 V (*vs.* Na/Na^+). Thus, the intercalated Na^+ above 1.4 V remains in the $Na_xV_2O_5$ lattice, and cannot be electrochemically extracted in the subsequent cycles. This is totally different from that of Li^+ intercalation in V_2O_5, which shows excellent reversibility for one Li^+ intercalation in per V_2O_5 unit cell [52–54]. This difference may be due to the much higher diffusion barrier of Na^+ in V_2O_5 (1.06 eV) than that of Li^+ diffusion (0.24 eV) [55]. The huge energy barrier for Na^+ migration prevents the extraction of Na^+ from V_2O_5 lattice. After CV measurement in the voltage range of 1.4–4.0 V, we performed CV test on the same electrode in an extended voltage range of 1.0–4.0 V as presented in Fig. 3c. It is found that Na^+ can be reversibly intercalated into the initially formed Na_xV_2O phase, and with the increase of CV number, both the reduction peak and oxidation peak broaden and gradually shift to high voltage due to the local structural rearrangement of active material during the initial cycling.

The charge storage mechanism of the electrode was illustrated by the CV data (Fig. 3d) and power-law equation: $i=a\times v^b$, in which i and v denote the peak current and scan rate, respectively; a and b are adjustable parameters. When the b value is close to 1, the sodium storage is mainly contributed from surface pseudocapacitance; when the b value is 0.5, the sodium storage is totally dominated by diffusion-controlled intercalation process [56]. The b value determined from the linear relationship between $\log(i)$ *versus* $\log(v)$ (Fig. 3e) is 0.64, implying that the sodium storage in the electrode is mainly dominated by diffusion-controlled intercalation process. This is dramatically different from the case of V_2O_5 nanoparticles (5–7 nm) encapsulated in nanoporous carbon that exhibits significant pseudocapacitance behavior during sodiation/desodiation processes [48]. For the diffusion-controlled process, the Na^+ chemical diffusion coefficient (D_{Na^+}) in the electrode can be evaluated according to the Randles-Sevcik equation (Equation (S1)). Based on the linear relationship between oxidation peak current and the square root of scan rate (Fig. 4f), the D_{Na^+} value corresponding to the oxidation peak is 4.81×10^{-12} cm^2 s^{-1}. This D_{Na^+} value is comparable to that of hydrated V_2O_5 nanosheets (2.59×10^{-13} cm^2 s^{-1}) [57], V_2O_5/graphene composites (1.14×10^{-13} cm^2 s^{-1}) [58], $Na_3V_2(PO_4)/C$ composite (2.18×10^{-12} cm^2 s^{-1}) [59], $NaV_6O_{15}\cdot nH_2O$ nanowires (4.03×10^{-14} cm^2 s^{-1}) [60], and carbon-coated NaV_6O_{15} nanotubes (3.10×10^{-13} cm^2 s^{-1}) [61].

To reveal the structural changes of the V_2O_5 single-crystalline nanowires during discharging and charging processes, *ex-situ* XRD were performed on the electrode at various discharge-charge states (Fig. 4). At the beginning of the first discharge (from state 1 to 3), the XRD peak positions remain unchanged but the peak intensity decreases drastically, implying that the sample still preserves the orthorhombic phase (α-V_2O_5) but accompanied by declined crystallinity. In the following discharge process from state 4 to 7, the diffraction peaks corresponding to the orthorhombic phase (α-V_2O_5) gradually disappear, and meantime a new phase, α'-$Na_xV_2O_5$ (JCPDS No. 24-1157, P21mn), gradually develops, suggesting the formation of a biphasic domain. The phase transition from α-V_2O_5 to α'-$Na_xV_2O_5$ due to electrochemical intercalation of Na^+ was also observed in the previous literatures [22,23,38]. Further discharging from state 7 to 10 and charging from state 10 to 16, the XRD patterns remain unchanged, implying that intercalation and extraction of Na^+ in this region proceed *via* a single-phasees (solid solution) reaction. In the following discharge/charge processes (from state 16 to 27), the identical XRD patterns shown in Fig. 4c demonstrate that the initially formed α'-$Na_xV_2O_5$ phase possesses a rather high structural stability, which leads to excellent cycling performance after the first cycle (Fig. 2a).

The variation of interlayer distance (c value calculated from (001) diffraction peak position) of the material in different discharge/charge states was also presented in Fig. 4a. For the initial discharging from state 1 to 3 (Stage I), the interlayer distance of the sample almost keeps the original value of ~4.37 Å. Further discharging from state 3 to 6, the interlayer distance expands gradually from ~4.37 to ~4.78 Å, reflecting the phase transition from α-$Na_xV_2O_5$ to α'-$Na_xV_2O_5$ upon Na^+ intercalation. From state 6 to 27, the interlayer distance shows negligible variation (only ~0.42% decrement from fully discharged state 22 to fully charged state 27). This result is in good agreement with the very little change (0.4%) of c parameter when 0.6 Na^+ is intercalated in the electrochemically formed α'-NaV_2O_5 [22]. Based on the above analysis, the sodium storage reaction mechanism in the V_2O_5 single-crystalline nanowires is proposed as follows: during the first discharge process, ~0.02 mol Na^+ can be intercalated in per α-V_2O_5 unit cell without changing the phase structure (Stage I as expressed in Equation (7)). Further Na^+ intercalation results in an irreversible phase transition from α-V_2O_5 to α'-$Na_{0.88}V_2O_5$ (Stage II as expressed in Equation (8)) accompanied with a swelling of interlayer distance from ~4.37 to ~4.78 Å. In the follow-

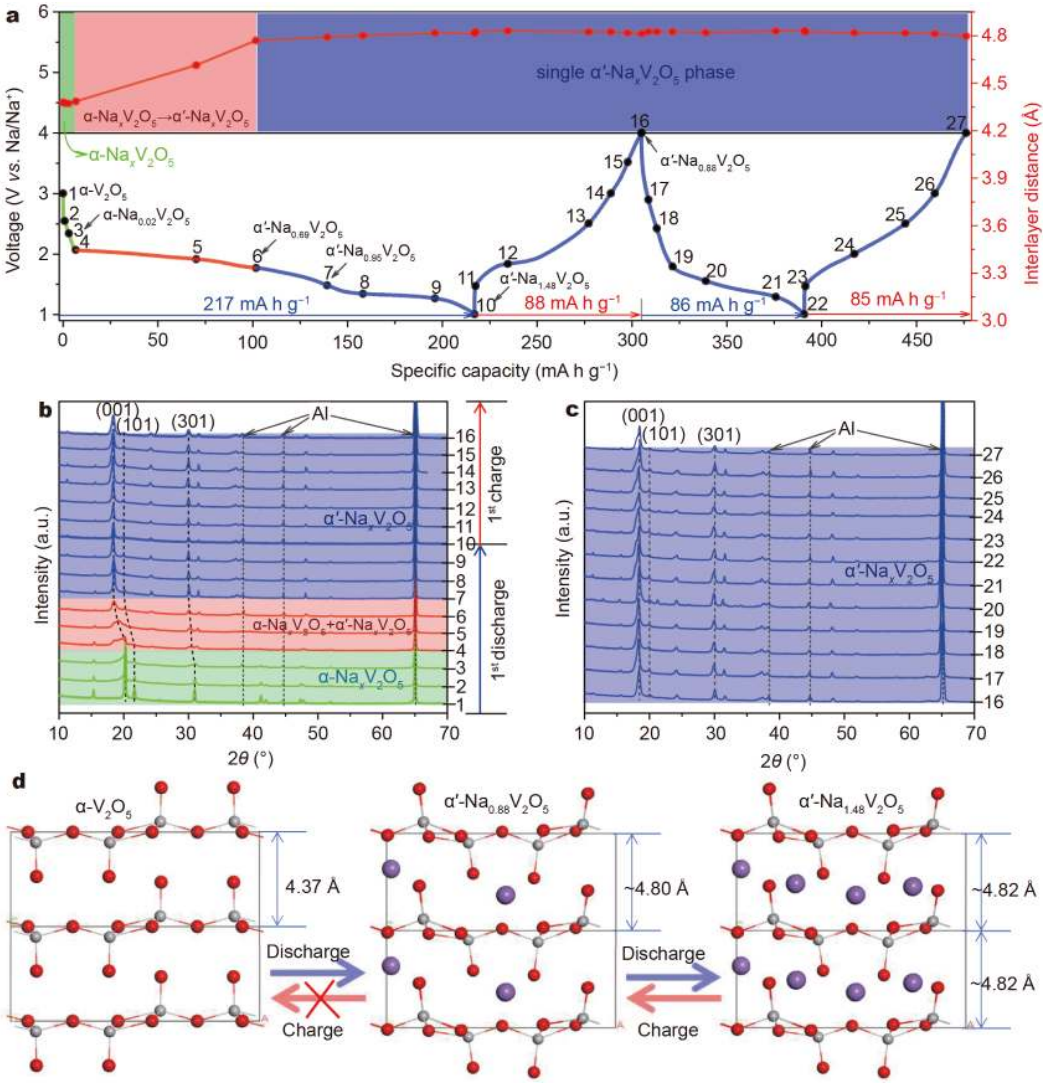

Figure 4 (a) The first cycle and second cycle discharge/charge profiles for the V_2O_5 nanowires electrode at a current density of 100 mA g^{-1}. (b, c) *Ex-situ* XRD patterns of the V_2O_5 nanowires electrode at different states in Fig. 4a. (d) Schematic illustration of the structural changes of V_2O_5 upon Na^+ intercalation and deintercalation.

ing discharge/charge processes, ~0.6 mol Na^+ can be reversibly intercalated in the initially formed α'-$Na_{0.88}V_2O_5$ through a single-phase reaction (Stage III as expressed in Equation (9)) with only ~0.42% variation of interlayer distance. The interlayer distance is determined by two competing forces: (i) the size exclusion and (ii) the electrostatic attraction between the inserted Na^+ and the V_2O_5 slab. Thus, the negligible change in the interlayer distance in Stage III is due to the offset of the two competitive interactions.

Stage I

$$\alpha\text{-}V_2O_5 + 0.02Na^+ + 0.02e^- \rightarrow \alpha\text{-}Na_{0.02}V_2O_5; \quad (7)$$

Stage II

$$\alpha\text{-}Na_{0.02}V_2O_5 + 0.86Na^+ + 0.86e^- \rightarrow \alpha'\text{-}Na_{0.88}V_2O_5; \quad (8)$$

Stage III

$$\alpha'\text{-}Na_{0.88}V_2O_5 + 0.60Na^+ + 0.60e^- \leftrightarrow \alpha'\text{-}Na_{1.48}V_2O_5. \quad (9)$$

The Na^+ storage behavior is totally different from that of Li^+ storage in V_2O_5. For Li^+ intercalation in V_2O_5, the $Li_xV_2O_5$ ($x \leq 2$) undergoes a series of phase transitions [18]: α(x<0.1), ε-phase $Li_xV_2O_5$ (0.35<x<0.7), δ-phase $Li_xV_2O_5$ (0.7<x<1.0), and γ-phase $Li_xV_2O_5$ (1.0<x<2.0), suggesting that Li^+ intercalation in V_2O_5 is more complex than that of Na^+; moreover, two Li^+ can be reversibly

intercalated/extracted from V_2O_5. These differences can be due to the larger ionic radius and higher electronic polarizability of Na^+ [62]. Larger ionic radius means higher migration barrier for ions, and therefore only partial intercalated Na^+ can be reversibly extracted from the $Na_xV_2O_5$ system. Higher electronic polarizability of the intercalated ion means larger deformation of its electronic distribution in the electric field generated by the ions of the V_2O_5 framework. Thus, the interaction of Na^+ induces relatively less structural changes of V_2O_5 framework as compared with Li^+ intercalation.

Ali *et al.* [19] investigated the Na^+ intercalation mechanism of the nanosized V_2O_5/C composite achieved by a ball-milling method and reported a rather different sodium intercalation behavior and mechanism. The nanosized V_2O_5/C composite shows a much higher initial charge capacity (293 mA h g^{-1}) than the initial discharge capacity (195 mA h g^{-1}). The fully discharged products of the nanosized V_2O_5 in the composite are crystalline NaV_2O_5 as a major phase and partially amorphous $Na_2V_2O_5$ as a minor phase; during the recharge process, Na^+ ions are extracted and orthorhombic V_2O_5 is recovered, but along with NaV_2O_5 as a minor phase. The difference between the reaction mechanisms of the single-crystalline V_2O_5 nanowires reported in this work and the nanosized V_2O_5/C composite is believed to be associated with the crystallinity of the two materials [49–51,63]. In the V_2O_5 single-crystalline nanowires, both the diffusion paths and intercalation sites for Na^+ are highly restricted in the long range well-ordered structure. While for the nanosized V_2O_5/C composite achieved by a ball-milling method, the nanosized V_2O_5 possesses large amounts of structural defects (such as unsaturated chemical bonds, vacancies, and structural disorders) and has higher Gibbs free energy than that of the V_2O_5 single-crystalline nanowires. These structural defects are highly reactive and could offer more sites for Na^+ intercalation and more open structure for Na^+ diffusion, which results in the reversible phase transition from V_2O_5 to NaV_2O_5 of the nanosized V_2O_5/C composite during discharge/charge cycling. Uchaker *et al.* [64] also found that amorphous V_2O_5 demonstrated superior Na^+ storage properties as compared with its crystalline counterparts, in terms of capacity, energy density, and cycling stability. Therefore, single-crystalline structure is not necessarily good for electrodes and fabricating highly defected and/or amorphous nanostructures are expected to be promising strategies, and worthy of further investigations for high-performance electroactive materials.

Fig. 5a, b present the typical GITT discharge/charge profiles of the V_2O_5 electrode in the 1st and 10th cycles. The typical potential profile of the electrode for a single titration (current pulse) is shown in Fig. 5e, in which both ΔE_s and ΔE_τ are labeled schematically. In both GITT profiles, the voltage response during consecutive current pulse exhibits a good linear relationship with the square root of pulse time ($\tau^{1/2}$) (Fig. 5f). In this case, the diffusion coefficient of Na^+ (D_{Na^+}) in the electrode can be calculated by the following equation [65,66]:

$$D_{Na^+}=\frac{4}{\pi\tau}\left(\frac{m_B V_M}{M_B S}\right)\left(\frac{\Delta E_s}{\Delta E_\tau}\right)^2 \quad (10)$$

where m_B, M_B and V_M are the mass, molar mass, and molar volume of active materials, respectively; S is the surface area of the electrode; ΔE_s is the change in open circuit voltage during the relaxation period; ΔE_τ is the total change in cell voltage during the current pulse time. The D_{Na^+} values of the electrode during the 1st and 10th discharge/charge cycles were calculated by Equation (10) based on the GITT profiles. As shown in Fig. 5c, during the initial discharge process, the D_{Na^+} values can be broadly divided into three regions. The first region is associated with the Na^+ intercalation in α-V_2O_5 as expressed by Equation (7); the D_{Na^+} value in this region decreases from 6.51×10^{-12} to 5.74×10^{-13} $cm^2\ s^{-1}$. The second region is associated with the phase transition reaction from α-$Na_{0.02}V_2O_5$ to α'-$Na_{0.02+x}V_2O_5$ due to further Na^+ intercalation as expressed by Equation (8); in this region, the D_{Na^+} value increases from 2.74×10^{-14} to 1.07×10^{-12} $cm^2\ s^{-1}$ due to the expanded interlayer distance of α'-$Na_xV_2O_5$ (Fig. 4a). In the third region, the D_{Na^+} value drops sharply from 8.75×10^{-13} to 1.12×10^{-14} $cm^2\ s^{-1}$, suggesting that Na^+ intercalation in this region is rather sluggish. During the first charge process (Fig. 5c), the D_{Na^+} value varies between 3.45×10^{-13} and 2.19×10^{-12} $cm^2\ s^{-1}$, much higher than that during the initial discharge process. At the end of the first charge process, the polarization of the electrode increases obviously and the D_{Na^+} value decreases sharply, implying that the extraction of Na^+ in this state becomes more and more difficult. Fig. 5d gives the D_{Na^+} of the electrode during the 10th discharge/charge cycles. The D_{Na^+} values between the 10th discharge and charge processes show a symmetric feature, indicating the superior electrochemical reversibility of the electrode. The D_{Na^+} values during the 10th cycle (corresponding to the reversible electrochemical reactions shown in Equation (8)) range from 10^{-12} to $10^{-11.5}$ $cm^2\ s^{-1}$, which is in accordance with the results (4.81×10^{-12} $cm^2\ s^{-1}$) from CV measurement (Fig. 3d). These D_{Na^+} values are significantly higher than

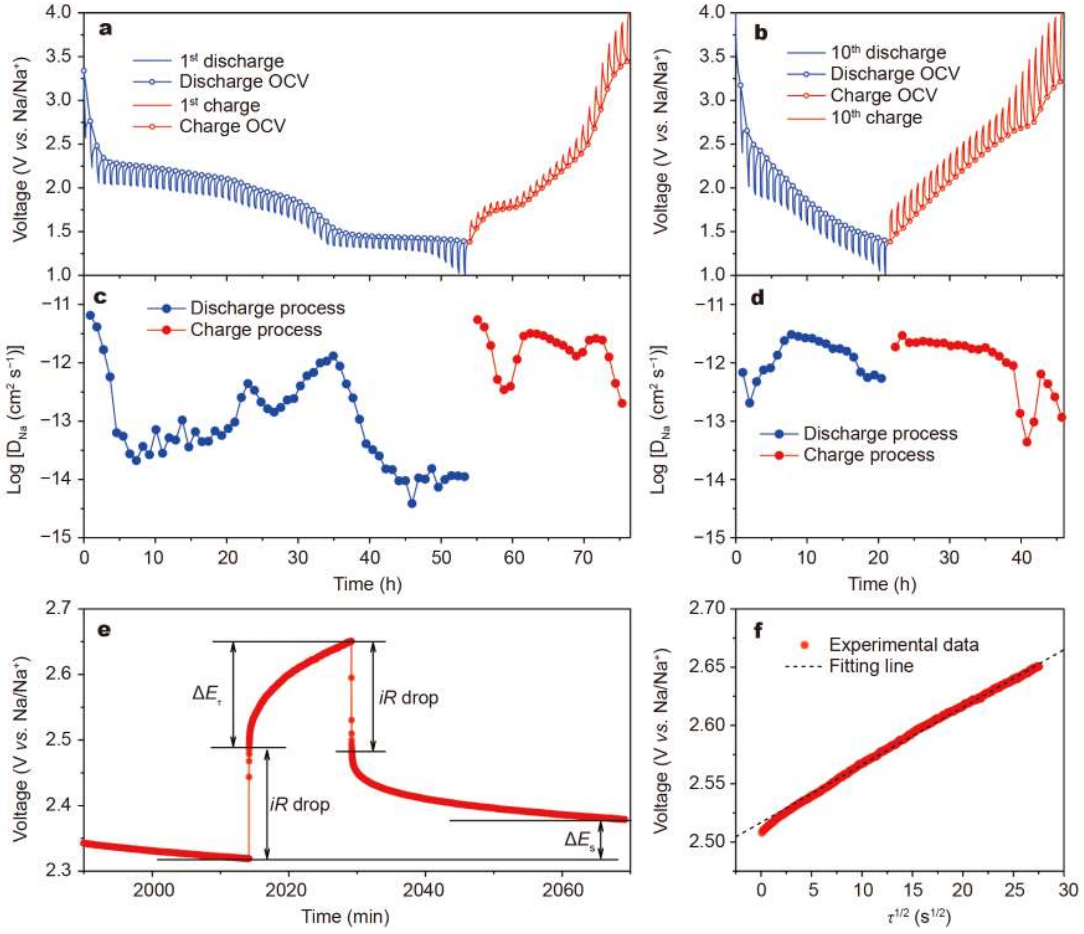

Figure 5 (a, b) GITT curves of the V_2O_5 nanowires electrodes during the first and tenth discharge/charge cycles as a function of time. (c, d) Na^+ diffusion coefficient (D_{Na^+}) calculated from the GITT data in Fig. 5a, b. (e) Typical potential profile of the electrode for a single titration (current pulse) step. (f) Linear relationship between the potential and the square root of pulse time ($\tau^{1/2}$).

those during the first discharge process, which can be attributed to the activation of the electrode upon the initial cycling. Because of the larger ionic radius of Na^+, the D_{Na^+} values are lower than the previous reported Li^+ diffusion coefficient in V_2O_5 (10^{-9}–10^{-10} cm^2 s^{-1}) [67]. The D_{Na^+} values are significantly higher than the previous reported value for Mg^{2+} diffusion coefficient in V_2O_5 (10^{-15} cm^2 s^{-1}) [68].

The morphology evolution of the electrode before cycling and after 100 cycles was observed by SEM as illustrated in Fig. 6a–f. Before cycling, the V_2O_5 nanowires are uniformly loaded on the as-prepared electrode (Fig. 6a–c). After 100 discharge/charge cycles at the current density of 100 mA g^{-1}, the nanowire morphology of the V_2O_5 sample is well retained (Fig. 6d–f), confirming the excellent structural integrity of the material during cycling. The TEM image (Fig. 6g) further verifies that the nanowire morphology is well preserved after 100 cycles; however, the surface of the V_2O_5 nanowires after 100 cycles gets coarse and the edge of the nanowires becomes blur as compared with the original nanowires (Fig. 1e, f). The SAED pattern (Fig. 6h) obtained from a typical nanowire shows a highly symmetrical dotted lattice, revealing the single-crystalline nature of the nanowires even after 100 cycles. The lattice fringe observed in HRTEM image (Fig. 6i) is about 0.34 nm, which can be ascribed to the (110) lattice plane of α′-$Na_xV_2O_5$. The HRTEM and SAED results are consistent with the *ex-situ* XRD patterns of the electrodes after different (the 1st, 3rd, 5th, and 100th) discharge/charge cycles (Fig. S4); with the cycle number increasing, the XRD patterns of the electrodes show negligible change and the α′-$Na_xV_2O_5$ (JCPDS No. 24-1157, P21mn) phase is well preserved even after 100 cycles. The superior stability of morphology and crystal

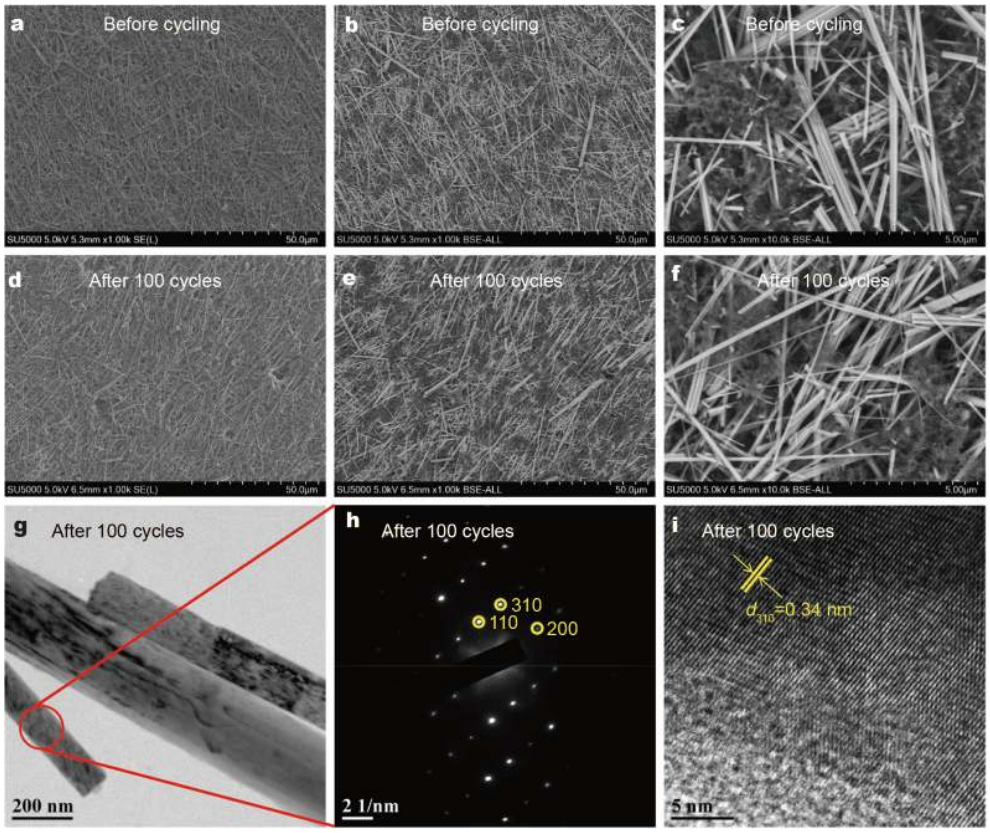

Figure 6 SEM images of the V_2O_5 nanowires electrodes (a–c) before cycling and (d–f) after 100 discharge/charge cycles. (g) TEM image, (h) SAED pattern, and (i) HRTEM image of the V_2O_5 nanowires after 100 discharge/charge cycles.

structure upon repeated sodiation/desodiation cycling accounts for the excellent cycling performance of the V_2O_5 nanowires electrode after the first cycle.

CONCLUSIONS

Orthorhombic V_2O_5 single-crystalline nanowires prepared by the hydrothermal method show a large initial discharge capacity of 217 mA h g^{-1} at a current density of 100 mA g^{-1}; however, there is an appreciable irreversible capacity loss with a rather low CE of 40.5%. After the first cycle, the electrode exhibits excellent cycling performance with a fading rate of 0.09% per cycle and a specific discharge capacity of 78 mA h g^{-1} at the 100th cycle. The initial Na^+ intercalation into the V_2O_5 single-crystalline nanowires was found to induce an irreversible phase transition from α-V_2O to α'-$Na_xV_2O_5$ (x<0.88), accompanied with an expanded interlayer distance from ~4.37 to ~4.80 Å; notably, the Na^+ in α'-$Na_xV_2O_5$ (x<0.88) cannot be electrochemically extracted, leading to the large irreversible capacity loss during the initial discharge/charge cycle in addition to the formation of SEI; however, Na^+ can be reversibly inserted into the α'-$Na_{0.88}V_2O_5$ *via* a single-phase (solid solution) reaction with a negligible variation of the interlayer distance of the host structure, consequently leading to the excellent cycling performance of the electrode after the 1st discharge/charge cycle. The Na^+ diffusion coefficient during the first discharge process ranges from 10^{-14} to 10^{-12} cm^2 s^{-1}; after the first discharge process, the Na^+ diffusion coefficient of the electrode significantly increases (10^{-12}–$10^{-11.5}$ cm^2 s^{-1}) due to the expanded interlayer distance of the α'-$Na_xV_2O_5$. Single-crystalline electrodes are not necessarily the best for electrochemical intercalation; highly defective and/or amorphous nanostructures with more open diffusion paths and intercalation sites are favorable for attaining high transport kinetics and storage capacity.

Received 8 June 2020; accepted 21 July 2020; published online 13 October 2020

1 Zubi G, Dufo-López R, Carvalho M, *et al.* The lithium-ion battery: State of the art and future perspectives. Renew Sustain Energy Rev, 2018, 89: 292–308

2 Li M, Lu J, Chen Z, *et al.* 30 Years of lithium-ion batteries. Adv Mater, 2018, 30: 1800561
3 Massé RC, Uchaker E, Cao G. Beyond li-ion: Electrode materials for sodium- and magnesium-ion batteries. Sci China Mater, 2015, 58: 715–766
4 Vaalma C, Buchholz D, Weil M, *et al.* A cost and resource analysis of sodium-ion batteries. Nat Rev Mater, 2018, 3: 18013
5 Hwang JY, Myung ST, Sun YK. Sodium-ion batteries: Present and future. Chem Soc Rev, 2017, 46: 3529–3614
6 Su H, Jaffer S, Yu H. Transition metal oxides for sodium-ion batteries. Energy Storage Mater, 2016, 5: 116–131
7 Sun Y, Guo S, Zhou H. Exploration of advanced electrode materials for rechargeable sodium-ion batteries. Adv Energy Mater, 2018, 9: 1800212
8 Liu Q, Hu Z, Chen M, *et al.* Recent progress of layered transition metal oxide cathodes for sodium-ion batteries. Small, 2019, 15: 1805381
9 Zhao LN, Zhang T, Zhao HL, *et al.* Polyanion-type electrode materials for advanced sodium-ion batteries. Mater Today Nano, 2020, 10: 100072
10 Qian J, Wu C, Cao Y, *et al.* Prussian blue cathode materials for sodium-ion batteries and other ion batteries. Adv Energy Mater, 2018, 8: 1702619
11 Yin X, Sarkar S, Shi S, *et al.* Recent progress in advanced organic electrode materials for sodium-ion batteries: synthesis, mechanisms, challenges and perspectives. Adv Funct Mater, 2020, 30: 1908445
12 Wang Q, Xu J, Zhang W, *et al.* Research progress on vanadium-based cathode materials for sodium ion batteries. J Mater Chem A, 2018, 6: 8815–8838
13 Liu P, Zhu K, Gao Y, *et al.* Recent progress in the applications of vanadium-based oxides on energy storage: From low-dimensional nanomaterials synthesis to 3D micro/nano-structures and free-standing electrodes fabrication. Adv Energy Mater, 2017, 7: 1700547
14 Xu X, Xiong F, Meng J, *et al.* Vanadium-based nanomaterials: a promising family for emerging metal-ion batteries. Adv Funct Mater, 2020, 30: 1904398
15 Etman AS, Sun J, Younesi R. V_2O_5·nH_2O nanosheets and multi-walled carbon nanotube composite as a negative electrode for sodium-ion batteries. J Energy Chem, 2019, 30: 145–151
16 Dong J, Jiang Y, Wei Q, *et al.* Strongly coupled pyridine-V_2O_5·nH_2O nanowires with intercalation pseudocapacitance and stabilized layer for high energy sodium ion capacitors. Small, 2019, 15: 1900379
17 Cai Y, Fang G, Zhou J, *et al.* Metal-organic framework-derived porous shuttle-like vanadium oxides for sodium-ion battery application. Nano Res, 2018, 11: 449–463
18 Yao J, Li Y, Massé RC, *et al.* Revitalized interest in vanadium pentoxide as cathode material for lithium-ion batteries and beyond. Energy Storage Mater, 2018, 11: 205–259
19 Ali G, Lee JH, Oh SH, *et al.* Investigation of the Na intercalation mechanism into nanosized V_2O_5/C composite cathode material for Na-ion batteries. ACS Appl Mater Interfaces, 2016, 8: 6032–6039
20 West K. Sodium insertion in vanadium oxides. Solid State Ion, 1988, 28-30: 1128–1131
21 Su DW, Dou SX, Wang GX. Hierarchical orthorhombic V_2O_5 hollow nanospheres as high performance cathode materials for sodium-ion batteries. J Mater Chem A, 2014, 2: 11185–11194
22 Muller-Bouvet D, Baddour-Hadjean R, Tanabe M, *et al.* Electrochemically formed α'-NaV_2O_5: A new sodium intercalation compound. Electrochim Acta, 2015, 176: 586–593
23 Si H, Seidl L, Chu EML, *et al.* Impact of the morphology of V_2O_5 electrodes on the electrochemical Na^+-ion intercalation. J Electrochem Soc, 2018, 165: A2709–A2717
24 Zhai T, Liu H, Li H, *et al.* Centimeter-long V_2O_5 nanowires: From synthesis to field-emission, electrochemical, electrical transport, and photoconductive properties. Adv Mater, 2010, 22: 2547–2552
25 Zhou F, Zhao X, Yuan C, *et al.* Vanadium pentoxide nanowires: Hydrothermal synthesis, formation mechanism, and phase control parameters. Cryst Growth Des, 2007, 8: 723–727
26 Li Y, Yao J, Uchaker E, *et al.* Sn-doped V_2O_5 film with enhanced lithium-ion storage performance. J Phys Chem C, 2013, 117: 23507–23514
27 Yao JH, Yin ZL, Zou ZG, *et al.* Y-doped V_2O_5 with enhanced lithium storage performance. RSC Adv, 2017, 7: 32327–32335
28 Li Y, Liu C, Xie Z, *et al.* Superior sodium storage performance of additive-free V_2O_5 thin film electrodes. J Mater Chem A, 2017, 5: 16590–16594
29 Liu Y, Clark M, Zhang Q, *et al.* V_2O_5 nano-electrodes with high power and energy densities for thin film Li-ion batteries. Adv Energy Mater, 2011, 1: 194–202
30 Fontenot CJ, Wiench JW, Pruski M, *et al.* Vanadia gel synthesis *via* peroxovanadate precursors. 1. *In situ* laser Raman and ^{51}V NMR characterization of the gelation process. J Phys Chem B, 2000, 104: 11622–11631
31 Rui X, Tang Y, Malyi OI, *et al.* Ambient dissolution–recrystallization towards large-scale preparation of V_2O_5 nanobelts for high-energy battery applications. Nano Energy, 2016, 22: 583–593
32 Petkov V, Trikalitis PN, Bozin ES, *et al.* Structure of V_2O_5·nH_2O xerogel solved by the atomic pair distribution function technique. J Am Chem Soc, 2002, 124: 10157–10162
33 Dewangan K, Sinha NN, Chavan PG, *et al.* Synthesis and characterization of self-assembled nanofiber-bundles of V_2O_5: Their electrochemical and field emission properties. Nanoscale, 2012, 4: 645–651
34 Mai L, Xu L, Han C, *et al.* Electrospun ultralong hierarchical vanadium oxide nanowires with high performance for lithium ion batteries. Nano Lett, 2010, 10: 4750–4755
35 Takahashi K, Limmer SJ, Wang Y, *et al.* Synthesis and electrochemical properties of single-crystal V_2O_5 nanorod arrays by template-based electrodeposition. J Phys Chem B, 2004, 108: 9795–9800
36 Shi S, Cao M, He X, *et al.* Surfactant-assisted hydrothermal growth of single-crystalline ultrahigh-aspect-ratio vanadium oxide nanobelts. Cryst Growth Des, 2007, 7: 1893–1897
37 Pan S, Chen L, Li Y, *et al.* Disodium citrate-assisted hydrothermal synthesis of V_2O_5 nanowires for high performance supercapacitors. RSC Adv, 2018, 8: 3213–3217
38 Van Nghia N, Long PD, Tan TA, *et al.* Electrochemical performance of a V_2O_5 cathode for a sodium ion battery. J Electr Materi, 2017, 46: 3689–3694
39 Leger C, Bach S, Soudan P, *et al.* Structural and electrochemical properties of ω-$Li_xV_2O_5$ ($0.4 \leq x \leq 3$) as rechargeable cathodic material for lithium batteries. J Electrochem Soc, 2005, 152: A236
40 Li Y, Huang Y, Zheng Y, *et al.* Facile and efficient synthesis of α-Fe_2O_3 nanocrystals by glucose-assisted thermal decomposition method and its application in lithium ion batteries. J Power Sources, 2019, 416: 62–71

41 Huang Y, Li Y, Huang R, *et al.* Ternary $Fe_2O_3/Fe_3O_4/FeCO_3$ composite as a high-performance anode material for lithium-ion batteries. J Phys Chem C, 2019, 123: 12614–12622
42 Wang J, Luo N, Wu J, *et al.* Hierarchical spheres constructed by ultrathin VS_2 nanosheets for sodium-ion batteries. J Mater Chem A, 2019, 7: 3691–3696
43 Luo Y, Xu X, Tian X, *et al.* Facile synthesis of a $Co_3V_2O_8$ interconnected hollow microsphere anode with superior high-rate capability for Li-ion batteries. J Mater Chem A, 2016, 4: 5075–5080
44 Zhen M, Guo X, Gao G, *et al.* Rutile TiO_2 nanobundles on reduced graphene oxides as anode materials for Li ion batteries. Chem Commun, 2014, 50: 11915–11918
45 Liu X, Zhang J, Si W, *et al.* High-rate amorphous SnO_2 nanomembrane anodes for Li-ion batteries with a long cycling life. Nanoscale, 2015, 7: 282–288
46 Ou X, Li J, Zheng F, *et al. In situ* X-ray diffraction characterization of $NiSe_2$ as a promising anode material for sodium ion batteries. J Power Sources, 2017, 343: 483–491
47 Wei Q, Liu J, Feng W, *et al.* Hydrated vanadium pentoxide with superior sodium storage capacity. J Mater Chem A, 2015, 3: 8070–8075
48 Raju V, Rains J, Gates C, *et al.* Superior cathode of sodium-ion batteries: orthorhombic V_2O_5 nanoparticles generated in nanoporous carbon by ambient hydrolysis deposition. Nano Lett, 2014, 14: 4119–4124
49 Uchaker E, Cao G. The role of intentionally introduced defects on electrode materials for alkali-ion batteries. Chem Asian J, 2015, 10: 1608–1617
50 Maier J. Review—battery materials: Why defect chemistry? J Electrochem Soc, 2015, 162: A2380–A2386
51 Liu Y, Liu D, Zhang Q, *et al.* Engineering nanostructured electrodes away from equilibrium for lithium-ion batteries. J Mater Chem, 2011, 21: 9969–9983
52 Qin M, Liang Q, Pan A, *et al.* Template-free synthesis of vanadium oxides nanobelt arrays as high-rate cathode materials for lithium ion batteries. J Power Sources, 2014, 268: 700–705
53 Liang S, Hu Y, Nie Z, *et al.* Template-free synthesis of ultra-large V_2O_5 nanosheets with exceptional small thickness for high-performance lithium-ion batteries. Nano Energy, 2015, 13: 58–66
54 An Q, Wei Q, Zhang P, *et al.* Three-dimensional interconnected vanadium pentoxide nanonetwork cathode for high-rate long-life lithium batteries. Small, 2015, 11: 2654–2660
55 Carrasco J. Role of van der Waals forces in thermodynamics and kinetics of layered transition metal oxide electrodes: alkali and alkaline-earth ion insertion into V_2O_5. J Phys Chem C, 2014, 118: 19599–19607
56 Liu J, Wang J, Xu C, *et al.* Advanced energy storage devices: Basic principles, analytical methods, and rational materials design. Adv Sci, 2018, 5: 1700322
57 Liu C, Yao J, Zou Z, *et al.* Boosting the cycling stability of hydrated vanadium pentoxide by Y^{3+} pillaring for sodium-ion batteries. Mater Today Energy, 2019, 11: 218–227
58 Wang L, Wang Y, Zhao Y. Freeze-drying method to synthesize V_2O_5/graphene composites toward enhanced sodium ion storage. Ceramics Int, 2018, 44: 23279–23283
59 Lim SJ, Han DW, Nam DH, *et al.* Structural enhancement of $Na_3V_2(PO_4)_3$/C composite cathode materials by pillar ion doping for high power and long cycle life sodium-ion batteries. J Mater Chem A, 2014, 2: 19623–19632
60 Shang C, Hu L, Lin Q, *et al.* Integration of $NaV_6O_{15}{\cdot}nH_2O$ nanowires and rGO as cathode materials for efficient sodium storage. Appl Surf Sci, 2019, 494: 458–464
61 Song X, Li J, Li Z, *et al.* Superior sodium storage of carbon-coated NaV_6O_{15} nanotube cathode: pseudocapacitance *versus* intercalation. ACS Appl Mater Interfaces, 2019, 11: 10631–10641
62 Pereira-Ramos JP, Messina R, Perichon J. Electrochemical formation of vanadium pentoxide bronzes $M_xV_2O_5$ in molten dimethylsulfone. J Electrochem Soc, 1988, 135: 3050–3057
63 Ma W, Zhang C, Liu C, *et al.* Impacts of surface energy on lithium ion intercalation properties of V_2O_5. ACS Appl Mater Interfaces, 2016, 8: 19542–19549
64 Uchaker E, Zheng YZ, Li S, *et al.* Better than crystalline: Amorphous vanadium oxide for sodium-ion batteries. J Mater Chem A, 2014, 2: 18208–18214
65 Zhu Y, Gao T, Fan X, *et al.* Electrochemical techniques for intercalation electrode materials in rechargeable batteries. Acc Chem Res, 2017, 50: 1022–1031
66 Weppner W, Huggins RA. Determination of the kinetic parameters of mixed-conducting electrodes and application to the system Li_3Sb. J Electrochem Soc, 1977, 124: 1569–1578
67 Lee JH, Kim JM, Kim JH, *et al.* Toward ultrahigh-capacity V_2O_5 lithium-ion battery cathodes *via* one-pot synthetic route from precursors to electrode sheets. Adv Mater Interfaces, 2016, 3: 1600173
68 Attias R, Salama M, Hirsch B, *et al.* Solvent effects on the reversible intercalation of magnesium-ions into V_2O_5 electrodes. ChemElectroChem, 2018, 5: 3514–3524

Acknowledgements This work was financially supported by the National Natural Science Foundation of China (51664012), Guangxi Natural Science Foundation (2017GXNSFAA198117 and 2015GXNSFGA139006), and the Technology Major Project of Guangxi (AA19046001).

Author contributions Li Y, Yao J, and Cao G conceived the idea and data analysis. Ji J and Zhang Y performed the experiments. Li Y and Yao J wrote the paper with support from Cao G. Huang B helped to discuss partial experimental data. All authors contributed to the general discussion.

Conflict of interest The authors declare no conflict of interest.

Supplementary information Experimental details and supporting data are available in the online version of the paper.

Yanwei Li is a professor at the College of Chemistry and Bioengineering, Guilin University of Technology. He received his PhD from Harbin Institue of Technology in 2007. His current research interests lie in the design, synthesis, and characterization of advanced materials for Li/Na/Mg-ion batteries.

Jinhuan Yao is a professor at the College of Chemistry and Bioengineering, Guilin University of Technology. She received her PhD in chemical technology from Guangxi University in 2013. Her current research interests focus on the synthesis of metal oxides and their composites for energy storage devices.

Guozhong Cao is a Boeing-Steiner professor of materials science and engineering, professor of chemical engineering and adjunct professor of mechanical engineering at the University of Washington. He is one of Thomson Reuters Highly Cited Researchers and his current research is focused on chemical processing of nanomaterials for solar cells, batteries, and supercapacitors as well as actuators and sensors for aviation and biomedical applications.

正交相V_2O_5单晶纳米线的钠离子存储性能及机理研究

李延伟[1,2], 季靖程[1], 姚金环[1*], 张颖[1], 黄斌[1], 曹国忠[2*]

摘要 深入理解电极的电化学反应过程和机理对高性能电极材料的设计、开发至关重要. 本文研究了正交相V_2O_5单晶纳米线在1.0–4.0 V (*vs*. Na/Na^+)电位窗口下的钠离子存储行为和机理. 该单晶纳米线在首次放电/充电循环中表现出高的不可逆容量损失, 在随后的循环中表现出良好的循环稳定性. 在100 mA g^{-1}电流密度下, 其初始放电和充电比容量分别为217和88 mA h g^{-1}, 对应的库伦效率仅为40.5%. 经过100次循环后, 其可逆放电容量保持在78 mA h g^{-1}, 与第二次放电容量相比其每圈循环衰减率仅为0.09%. 采用循环伏安(CV)、非原位X-射线衍射(*ex-situ* XRD)、扫描电镜(SEM)和透射电镜(TEM)表征, 分析了正交相V_2O_5单晶纳米线的钠离子存储机理, 发现V_2O_5单晶纳米线在首次循环中的高不可逆容量损失主要是因为其在放电过程中生成了钠离子无法脱出的α'-$Na_xV_2O_5$ ($0.02 < x < 0.88$) 单晶相. 该α'-$Na_{0.88}V_2O_5$可通过单相(固溶体)反应可逆地嵌入和脱出钠离子, 因此在后续循环中表现出优异的稳定性. 采用恒电流间歇电位滴定(GITT)分析发现, α'-$Na_xV_2O_5$中钠离子扩散系数值为10^{-12}–$10^{-11.5}$ cm^2 s^{-1}.